

A Critical Analysis of Rayleigh-Taylor Growth Rates

J. Glimm^{**1 2}, J. W. Grove^{†3}, X. L. Li^{*1}, W. Oh^{*1}, D. H. Sharp^{‡4}

^{*}*Department of Applied Mathematics and Statistics, University at Stony Brook, Stony Brook, NY 11794-3600;*

^{*}*Center for Data Intensive Computing, Brookhaven National Laboratory, Upton NY 11793-6000;*

[†]*Hydrodynamics Methods Group, Applied Physics Division, Los Alamos National Laboratory, Los Alamos, NM 87545;*

[‡]*Complex Systems Group, Theoretical Division, Los Alamos National Laboratory, Los Alamos, NM 87545*

E-mail: glimm@ams.sunysb.edu; jgrove@lanl.gov; linli@ams.sunysb.edu; woh@ams.sunysb.edu; and dhs@t13.lanl.gov

Received TBA

Recent simulations of Rayleigh-Taylor instability growth rates display considerable spread. We propose that differences in numerical dissipation effects (mass diffusion and viscosity) due to algorithmic differences and differences in simulation duration are the dominant factors that produce such different results. Within the simulation size and durations explored here, we have explained principal discrepancies as due to numerical dispersion through comparison of simulations using different algorithms. Furthermore, we have tentatively identified viscosity as having the larger role of these two dissipative effects over the time range examined here.

We present new 3D front tracking simulations that show agreement with the range of reported experimental values.

We begin an exploration of new physical length scales, that may characterize a transition to a new Rayleigh-Taylor mixing regime.

1. INTRODUCTION

1.1. Purpose and Scope of the Paper

Accurate numerical simulation of multiphase fluid mixing rates is a long standing challenge for computational fluid dynamics. Only recently has the available hardware allowed significant three dimensional studies. We consider here one of the most important of this class of problems, Rayleigh-Taylor instability. Rayleigh-Taylor in-

¹Supported in part by the Applied Mathematics Subprogram of the U.S. Department of Energy DE-FG02-90ER25084, DE-FG02-989ER2536, DE-FG03-98DP00206

²Supported in part by the Department of Energy Office of Inertial Fusion, the Army Research Office, grant DAAG559810313, The National Science Foundation, grant DMS-9732876, and Los Alamos National Laboratory

³Supported by the U.S. Department of Energy

⁴Supported by the US Department of Energy under contract W-7405-ENG-36

stability results when a randomly perturbed density contrast interface is subject to continuous acceleration. A basic characteristic of Rayleigh-Taylor instability is the constant that describes the acceleration of the mixing zone edge.

A wide range of values for this acceleration constant have been reported on the basis of simulation studies, some of which fall outside the limits of experimental error. The purpose of this paper is to begin a systematic analysis of causes of these discrepancies. To do this, we summarize the results of previous Rayleigh-Taylor instability studies, identify potential sensitive factors in Rayleigh-Taylor simulations, and report on new simulation results designed to quantify the effects of a number of these factors.

There are three main results in this paper. The first is to show that front tracking simulations using the *FronTier* code are in agreement with experimental results. To do this it is necessary to correct for finite compressibility effects and to compensate for different conventions in the definition of the growth rate.

The second main result is to identify a possible cause for the spread in simulation results. We compare distinct algorithms, paying special attention to dissipative effects. Over the simulation time and size considered here, we can duplicate the observed spread in simulation growth rates through comparison of capturing to tracking algorithms. Restricting to typical high and low values of the growth rate, there is approximately a factor of two to be explained. The low values of the growth rate are time dependent, and about half of this factor of two difference in simulations occurs during the simulation times reported in this paper. For simulations with identical gridding, simulation time, and other numerical parameters, we see a 40% decrease in the growth rate for capturing algorithms with artificial dissipation, as compared to *FronTier*, which completely eliminates dissipation for interfacial vorticity and for density discontinuities. Thus essentially all of this discrepancy, for the times studied here, can be attributed to interfacial dissipative mechanisms in capturing algorithms. Moreover, we can tentatively identify viscosity rather than mass diffusion as the dominant cause through comparison of two capturing codes, one of which is designed to control mass diffusion while the other is not.

The third main result of this paper is an initial exploration of a possible new physics regime for Rayleigh-Taylor mixing, through identification of a new length scale that is independent of the mixing zone width.

All studies in this paper need to be taken to later time, as it is known that the discrepancies increase strongly with time.

1.2. Background Discussion of Rayleigh-Taylor Instability

An interface between fluids of different densities is unstable when subjected to an acceleration directed from the heavy fluid to the light fluid [31, 38, 35]. This instability, known as Rayleigh-Taylor instability, has been a challenge to computational fluid dynamics since the early days of computers [5]. The instability has a fingering nature, with bubbles of light fluid rising into the ambient heavy fluid and spikes of heavy fluid falling into the light fluid. With $\rho_1 < \rho_2$ representing the light and heavy fluid densities, and the Atwood number $A = (\rho_2 - \rho_1)/(\rho_2 + \rho_1)$ a buoyancy renormalization to gravity g , the outer edges of the mixing zone $Z_k(t)$

are observed to obey the large time asymptotic scaling law

$$Z_k(t) = (-1)^k \alpha_k A g t^2 \quad (1)$$

where α_k is a constant. Here, to be consistent with the conventions of laboratory experiments, the acceleration (gravity) is directed along the negative z axis, so that bubbles “fall” downward, spikes rise, and $Z_1 < 0$.

Rayleigh-Taylor instability arises in a variety of applications, ranging from incompressible regimes such as wind shears in thunder shower systems to highly compressible flows as occur in inertial confinement fusion and in supernovas. For this reason, the use of two fluid Euler equations to model the fluid flow is appropriate. Laboratory experiments are nearly incompressible. There are four principal numerical difficulties.

1. The sharp interface between the distinct fluids is difficult to maintain for most Eulerian algorithms;
2. The geometric complexity of the late time unstable interface between the fluids is a source of difficulty for most Lagrangian algorithms;
3. The requirement for a fully compressible code which can be validated on nearly incompressible experiments imposes a strain on computational resources and algorithms;
4. The spatial complexity and late time simulations required to observe a well developed self similar flow regime pose a challenge in terms of simulation resources and algorithmic efficiency.

1.3. Summary of Rayleigh-Taylor Results

The bubble acceleration constant $\alpha_b \equiv \alpha_1$ provides the most basic characterization of the mixing zone. However as Table 1 illustrates, simulations show considerable spread in reported values for α_b . Results from four independent series of experiments show a spread (including error bars) of nearly a factor of two. Somewhat over half of this spread is due to systematic differences among the four series of experiments; the error bars reported for each single experiment account for the remainder. Theoretical results are generally consistent with the experiments. The simulation results have a spread of a factor of about six, with the lower values of α_b falling outside the estimates of experimental error. Most of these simulations give growth rates which lie within a factor of 2.5 of one another. The spread in simulation values has widened as increased computational resources have allowed exploration of larger spatial ensembles of random modes, carried to later times. Plainly, there is a need for an analysis of the simulation results and their algorithmic basis which can explain the spread in simulation values. There is also a need for simulation or other studies of the experiments to explain the spread in experimental values. The present paper is a beginning of such a study, with a focus on algorithmic issues.

1.4. Outline of Paper

In Sec. 2 we discuss the algorithmic and simulation factors that have been suspected of influencing the simulation values of α_b . The dissipative mechanisms of

TABLE 1
Determination of α_b by experiment, theory and simulation

Theory: Bubble Merger Models			
Sharp/Wheeler [36], Sharp [35]	'61	$\alpha_b \sim 0.01 - 0.025$	3D
Glimm/Sharp [20], Zhang [43]	'90	$\alpha_b \sim 0.06$	2D
Alon <i>et al.</i> [3]	'94	$\alpha_b \sim 0.05$	2D
Glimm/Sharp [21]	'98	$\alpha_b \sim 0.045$	2D
Cheng/Glimm/Sharp [7]	'99	$\alpha_b \sim 0.06$	3D
Experiments			
Read/Youngs [32, 40]	'84	$\alpha_b \sim 0.58 - 0.65$	2D
		$\alpha_b \sim 0.063 - 0.077$	3D
Kucherenko <i>et al.</i> [24]	'91	$\alpha_b \sim 0.07$	3D
Snider/Andrews [37]	'94	$\alpha_b \sim 0.07 \pm 0.007$	3D
Schneider/Dimonte/Remington [34]	'99	$\alpha_b \geq 0.054$	3D
Dimonte/Schneider [11]	'99	$\alpha_b \sim 0.05 \pm 0.01$	3D
Simulation			
Youngs [41]	'91	$\alpha_b \sim 0.04 - 0.05$	3D
Youngs [42]	'99	$\alpha_b \sim 0.03$	3D
S.-Y. Chen	'99	$\alpha_b \sim 0.043$	3D
Dimits <i>et al.</i> (PPM) [10]	'99	$\alpha_b \sim 0.016$	3D
Cheng/Glimm/Li/Sharp [7]	'99	$\alpha_b \sim 0.08$	3D
Glimm/Grove/Li/Oh/Sharp (this work)	'99	$\alpha_b \sim 0.07$	3D
Oparin [29]	'99	$\alpha_b \sim 0.075$	3D

mass diffusion and viscosity (vorticity diffusion) are known to be important sources of numerical errors for flows with material interfaces. To assess and differentiate between the two dissipative mechanisms of mass and vorticity diffusion, we employ an artificial compression algorithm, which controls mass diffusion but does not limit vorticity diffusion. In Sec. 3, we review the front tracking algorithm used in later sections of this paper. This algorithm is free from interfacial dispersion. Sec. 4 presents and analyzes new simulation studies. The purpose of the simulations and their analysis is to shed light on the role of potentially sensitive factors discussed in Sec. 2, and to show that *FronTier* simulations do in fact agree with experiment. Conclusions are stated in Sec. 5.

2. PRINCIPAL FACTORS AFFECTING SIMULATION RESULTS

2.1. The Numerical Analysis of Mass and Vorticity Diffusion

This paper presents evidence suggesting that numerical dissipation, primarily mass diffusion and viscosity, is the dominant error contributing to the discrepancy between simulations and experiments. Density contrasts and vorticity are concentrated along the interface, and so this is where capturing schemes concentrate their errors. Numerical dissipation is exacerbated in Rayleigh-Taylor instability simulations by the long time of the simulation, by the dynamically growing interface length along which the numerical dissipation occurs, and by the dominant role that the density contrasts and vorticity concentrations along the interface play in the growth of the mixing zone.

2.1.1. Physical Values of Mass Diffusivity

The influence of diffusion on small amplitude Rayleigh-Taylor exponential growth rates was analyzed in [13] using an Argon-Helium mixture, with a diffusion constant $D = 0.64 \text{ cm}^2/\text{sec}$. A reduction of the small amplitude exponential growth rate of about 20% was observed due to physical diffusivity. For comparison, fluid diffusivities are much smaller, on the order of $10^{-4} \text{ cm}^2/\text{sec}$, and should not influence experimental Rayleigh-Taylor growth rate values.

2.1.2. Estimates of Numerical Diffusivity

Numerical diffusion and dispersion are known to be serious issues for Eulerian finite difference algorithms. In the case of a Rayleigh-Taylor instability, where the instability is driven by density contrasts, these effects can be expected to be significant. Some insight into these effects can be gained by an investigation of the modified partial differential equations [33, 23, 39, 22, 25] for finite difference schemes for solving the linear advection equation

$$u_t + vu_x = 0. \quad (2)$$

This equation can be regarded as a model of the contact discontinuity mode for gas dynamics. For simplicity we assume $v > 0$ and consider schemes using flux limiting between the Lax-Wendroff method and upwind differencing. Following the notation of LeVeque [25] these schemes are of the form

$$u_j^{n+1} = u_j^n - \frac{\Delta t}{\Delta x} \left(f_{j+\frac{1}{2}}^n - f_{j-\frac{1}{2}}^n \right) \quad (3)$$

where

$$f_{j+\frac{1}{2}}^n = vu_j + \frac{1}{2}v(1-\nu)\phi_j(u_{j+1} - u_j), \quad (4)$$

$\nu = v\Delta t/\Delta x$, and the limiter ϕ_j is given by

$$\phi_j = \phi(\theta_j) \text{ and } \theta_j = \frac{u_j - u_{j-1}}{u_{j+1} - u_j}.$$

Such schemes are second order accurate provided $\phi(1) = 1$. We also observe that the CFL condition requires that $\nu < 1$.

For the unlimited case $\phi(\theta) \equiv 1$, where this scheme reduces to the Lax-Wendroff method, Richtmyer and Morton [33] state that solutions to the modified partial

differential equation

$$u_t + vu_x = -\frac{1}{6}v\Delta x^2(1-\nu^2)u_{xxx} - \frac{1}{8}v\Delta x^3\nu(1-\nu^2)u_{xxxx}. \quad (5)$$

are fourth order solutions to the finite difference scheme (3). More generally, for schemes with smooth $\phi(\theta)$, a straightforward but tedious computation yields a modified equation of the form

$$u_t + vu_x = \Delta x c_1(x, t)u_{xx} + \Delta x^2 c_2(x, t)u_{xxx} + \Delta x^3 c_3(x, t)u_{xxxx} \quad (6)$$

where

$$\begin{aligned} c_1(x, t) &= \frac{1}{2}v(1-\nu)(1-\phi(1)) \\ c_2(x, t) &= -\frac{1}{6}v(1-\nu)(1+\nu(3\phi(1)-2)-3\phi'(1)) \\ c_3(x, t) &= v(1-\nu) \left\{ \frac{1}{4}\phi''(1) \frac{u_{xx}^2 - 2u_x u_{xxx}}{u_x^2} u_{xx} - \right. \\ &\quad \left. \left(\frac{\nu + \nu^2 + 2(1-2\nu)\phi'(1)}{8} + \chi \frac{(1+6\nu^2)}{24} + \chi^2 \frac{\nu(1-\nu)}{8} \right) u_{xxxx} \right\} \end{aligned}$$

and $\chi = \phi(1) - 1$.

For the first order upwind method, where $\phi(\theta) \equiv 0$ the modified equation has a leading order diffusion coefficient equal to

$$D = \frac{1}{2}v(1-\nu)\Delta x u_{xx}. \quad (7)$$

As a model for gas dynamics the CFL condition requires that $(|v| + c)\Delta t/\Delta x < 1$. Here c is the sound speed. For the low compressibility flows of concern here, we can estimate a typical flow velocity as $|v| \approx 0.1c$ so that ν is on the order of a tenth or less. Translating grid units into physical units, with a 1 mm zoning and a time scale of seconds we find a numerical diffusion on the order of $0.005c$ cm²/sec. One physical interpretation of this quantity is the viscous diffusion of velocity fluctuations (vorticity) in a fluid with mean velocity v . For materials such as air or water, the physical values of the viscosity are well know and are available in such handbooks as the CRC Handbook of Chemistry and Physics. Comparing the ratios of the numerical to physical viscosities we see that the numerical viscosity of air is approximately three orders of magnitude greater than the physical viscosity while the numerical viscosity of water is approximately five orders of magnitude greater than its physical viscosity at approximately room temperature. Another interpretation is as the physical diffusion of one material into another. Again referring to the CRC Handbook we see that typical values for diffusivities of gases into liquids and various solutes into water are on the order of 10^{-5} – 10^{-4} cm²/sec while the diffusivities of various gases into air are on the order of 10^{-1} – 1 cm²/sec. Again comparing these coefficients to the numerical diffusivities above we see that the numerical diffusion coefficients are anywhere from six to eight orders of magnitude

greater than the physical diffusivity for solutes in water and from two to four orders of magnitude greater for the diffusion of gases into air. Reduction of D to its physical value for any of the above models would require refining the zoning by up to a factor of 10^8 in the worst case with a corresponding increase in computational effort of $10^{(d+1)f}$ for a refinement factor of 10^f in $d = 1, 2$, or 3 space dimensions, a route plainly not feasible for any but the simplest of the above cases.

The estimates described in the previous paragraph are in fact overly pessimistic. Second order methods, where $\phi(1) = 1$, eliminate the first order diffusion terms in the finite difference equations making the above order of magnitude estimates inappropriate. For such methods, in regions bounded away from spatial extrema in $u(x, t)$ and for Δx sufficiently small, the dominant term in equation (6) is the linear dispersion term

$$-\frac{1}{6}v\Delta x^2(1-\nu)(1+\nu-3\phi'(1))u_{xxx}. \quad (8)$$

While these methods are all formally second order accurate, for finite meshes the limiter will reduce to a locally first order method in regions of strong flow gradients such as at jumps or at corners. However, near such regions, numerical diffusion will smooth out the steep gradients and hence decrease the influence of the limiter. It is important to note that the effect of the dispersion term on the discrete solution to the second order method is qualitatively different from the effect of diffusion on the first order method. The former leads to the dispersion of oscillations without damping their amplitudes, while the latter reduces the amplitude of the oscillations as they diffuse. The diffusion in the numerical solution arises from the fourth order terms in (6). It is interesting to note that for a non-trivial limiter these diffusion terms are nonlinear.

For finite Δx , near jumps or corners, the finite difference solution behaves as a first order equation with a $t^{1/2}$ rate of spreading. Once the discrete Laplacian $u_{j-1} - 2u_j + u_{j+1}$ is $\mathcal{O}(\Delta x^2)$, the higher order analysis of the limiters is applicable and the subsequent dispersion scales as $t^{1/3}$. This scaling is observed in numerical experiments [26], where the width is observed to be approximately $(4/3)t^{1/3}$. If this subdiffusive dissipation is modeled by a grid dependent diffusivity as in Sec. 2.1.2, then the grid dependent diffusivity D must also be time dependent and scale as $t^{-1/6}$.

2.1.3. Numerical Diffusion Using Artificial Compression

We refer to [26] for a discussion of the flux limited scheme with artificial compression. In this scheme, the numerical mass diffusion is limited to about 2.5 cells, according to numerical experiments on the linear advection equation conducted in [26]. The nonlinear fluids simulations of Sec 4.2 show a larger diffusion length of about 6 – 7 cells.

The scheme has the same conservation form as equation (3), with the flux $f_{j+\frac{1}{2}}$ is defined as

$$f_{j+\frac{1}{2}} = \frac{1}{2} \left(vu_j^n + vu_{j+1}^n + g_j^n + g_{j+1}^n + L_j^n + L_{j+1}^n - |v + \gamma_{j+\frac{1}{2}}^n + \lambda_{j+\frac{1}{2}}^n| \Delta u_{j+\frac{1}{2}}^n \right) \quad (9)$$

and $\Delta u_{j+\frac{1}{2}}^n = u_{j+1}^n - u_j^n$. Here the vu terms in f generate a first order central difference scheme, the g 's define a total variation diminishing (TVD) [25] anti-diffusion term, and the L terms are artificial compression anti-diffusion. The terms proportional to $\Delta u_{j+\frac{1}{2}}^n$ are artificial viscosity terms. The first of these, proportional to v converts central differencing to upwind differencing. The role of γ is to control the g terms and likewise the λ terms regulate the L terms. Thus we define

$$\gamma_{j+\frac{1}{2}}^n = (g_{j+1}^n - g_j^n) / \Delta u_{j+\frac{1}{2}}^n \quad (10)$$

$$\lambda_{j+\frac{1}{2}}^n = (L_{j+1}^n - L_j^n) / \Delta u_{j+\frac{1}{2}}^n \quad (11)$$

if $\Delta u_{j+\frac{1}{2}}^n \neq 0$ and $\gamma_{j+\frac{1}{2}}^n = \lambda_{j+\frac{1}{2}}^n = 0$ otherwise.

The definitions

$$g_{j+\frac{1}{2}}^n = \frac{1}{2} \left(|v| - \frac{\Delta t}{\Delta x} v^2 \right) \Delta u_{j+\frac{1}{2}}^n, \quad (12)$$

$$g_j^n = M(g_{j-\frac{1}{2}}^n, g_{j+\frac{1}{2}}^n), \quad (13)$$

define a TVD scheme if $L = 0$, where

$$M = \text{sign } u_1 \min\{|u_1|, \dots, |u_r|\} \quad (14)$$

if all u_i have the same sign and $M = 0$ otherwise.

L is the artificial compression anti-diffusion. Let

$$L_{j+\frac{1}{2}}^n = \frac{1}{2} \left(|v| - \frac{\Delta t}{\Delta x} v^2 \right) \left[\Delta u_{j+\frac{1}{2}}^n - M(\Delta u_{j-\frac{1}{2}}^n, \Delta u_{j+\frac{1}{2}}^n, \Delta u_{j+\frac{1}{2}}^n) \right] \quad (15)$$

$$L_j^n = S \cdot \max \left(0, S \cdot M(\eta L_{j-\frac{1}{2}}^n, L_{j+\frac{1}{2}}^n), S \cdot M(L_{j-\frac{1}{2}}^n, \eta L_{j+\frac{1}{2}}^n) \right). \quad (16)$$

Here $S = \text{sign } L_{j+\frac{1}{2}}^n$ and

$$\eta = 2 \left| \frac{\left| \Delta u_{j-\frac{1}{2}}^n \right|^\beta - \left| \Delta u_{j+\frac{1}{2}}^n \right|^\beta}{\left| \Delta u_{j-\frac{1}{2}}^n \right|^\beta + \left| \Delta u_{j+\frac{1}{2}}^n \right|^\beta} \right|. \quad (17)$$

Note that both $\gamma_{j+\frac{1}{2}}^n$ and $\lambda_{j+\frac{1}{2}}^n$ are $\mathcal{O}(\Delta x)$ as $\Delta x \rightarrow 0$, so that the term in absolute values in equation (9) has the same sign as v for sufficiently small Δx . Thus, in the absence of the artificial compression terms, equation (9) is simply a generalization of equation (4) that encompasses both cases of $v > 0$ and $v < 0$ for the special choice of the flux limiter

$$\phi(\theta) = \phi_{\text{minmod}} = \begin{cases} 0 & \theta < 0, \\ \theta & 0 < \theta < 1, \\ 1 & 1 < \theta. \end{cases} \quad (18)$$

For $\eta = 0$, $L = 0$ and the scheme is TVD [25]. For $\eta = 2.5$ the diffusion width is shown [26] numerically to be about 2.5 cells wide, independent of the time t .

2.1.4. Transitions to New Flow Regimes

The sensitivity of multiphase flow to change of flow regime is well known [12]. The regime of a single length scale, for which the large scale structures are on the order of the width of the mixing zone, is known as chunk mix. Transitions to other flow regimes are characterized by introduction of one or more new length scales, to describe the probability distribution function (pdf) for the distribution of droplet and bubble sizes or fluid volume or mass fraction fluctuation length scales.

Additional fluid waves, such as shock waves, can cause shattering of large scale structures, and a change in flow regimes. They are thus a mechanism to cause a change of flow structure. The influence of dissipation to cause a change of flow regime was discussed in Sec. 2.1.2.

Continued acceleration leads to velocities growing without limit. In the presence of viscosity or compressibility, vorticity will diffuse off the interface to the interior flow, or will be generated there directly, giving rise to a transition to turbulent flow. Turbulent flows have an increased effective viscosity that decreases the observed values of α_b . Turbulent flow also drives turbulent effective diffusivity, leading to a further decrease in α_b . This range of issues has been considered by Youngs *et al.* in a series of papers, see for example [27, 9]. Numerical emulation of turbulent diffusion through numerical mass diffusion requires time dependent gridding, as diffusivity based upon a time increasing Reynolds number cannot otherwise match the observed $t^{-1/6}$ diffusivity for the TVD algorithm, as discussed in Sec. 2.1.2.

Experiments show between three and five generations of bubble merger. The lower bound comes from counting the decrease in the number of ripples or bubbles in the experimental plates of Read and Youngs. The upper bound five comes from the theory of most unstable wave length for these experiments. Over the time period of the experiments, the observed growth rate is very nearly linear in t^2 . Thus any transition to a new physical regime has not had an opportunity to influence α_b in this time period. Simulations do not exceed the lower bound of three generations of bubble merger. For this reason, any significant time dependence for α_b or any transition to a new flow regime that causes α_b to decrease in simulations is in disagreement with experiment.

2.2. Definition of the Statistical Ensemble

Wavelengths Present in Initial Perturbation. The self similar t^2 growth rate for the mixing zone thickness at late time results from the progressive merger of bubbles [21]. The bubbles individually achieve a terminal velocity due to a balance between buoyancy and drag, but as bubbles are removed from the edge of the mixing zone and neighbor bubbles expand to take their place in a merger process, the size dependent terminal velocity can increase. It is this continued increase in length scales which allows for continued acceleration.

To observe a universal value for α_b , it is desirable not to insert long wave lengths into the initial data, and thus to avoid contamination of the bubble merger mechanism with the growth at long wave lengths initially seeded in the initial data. A recommended convention is to choose wave lengths (Fourier modes) with wave-

length λ satisfying $\lambda \in [\lambda_{\min}, \lambda_{\max}]$ with $\lambda_{\min} = \lambda_{\max}/2$. Some authors include a further modulation and decrease the amplitude of the random modes near the edge of the allowed interval.

The modeling of an actual experiment, which will necessarily contain some level of unavoidable low frequency noise, gives a reason for simulations which do not follow the above restrictions on wavelengths λ present in the initial random interface. In [27], a simple analysis is given for the influence of long wave length “noise” as a small perturbation of a high wave length random surface. This work concludes that the influence is potentially significant and could increase the experimentally observed value of α_b . This analysis is based on a simple single mode computation. It would be desirable to repeat this analysis using full scale simulation.

Initial Amplitude of Perturbation. To avoid introduction of a new length scale into the problem, we want to choose the initial amplitude to be small, within the limit of accuracy of the small amplitude Rayleigh-Taylor theory. This small amplitude theory is then used for initialization, giving in effect a zero or infinitesimal initial amplitude. Most Eulerian finite difference schemes have trouble with initialization of small amplitude perturbations. Unless several zones are included within the initial amplitude of the perturbation, an Eulerian simulation with an untracked interface will have difficulty in observing and responding to the perturbation at all. This requirement leads to very fine scale zoning per initial wavelength or to use of large amplitude initial conditions. Front tracking, with its subgrid resolution, does not suffer from this problem. See Sec. 3.

Size of Statistical Ensemble of Initial Perturbations. The statistical ensemble converges to an infinite volume limit with surprising speed in two dimensional studies [6]. This issue has not been explored in three dimensions. The size, *i.e.*, the number of initial bubbles, is more important as a restriction on the duration of the simulation, since two or three generations of bubble merger reduce the number of bubbles by factors of 16 or 64, and the number of bubbles at the end of the simulation must still be enough for statistical significance. The requirement for two or three generations of bubble merger is to ensure that the simulation has entered the self similar regime and to explore the influence of numerical dissipation effects which could force a transition to a new flow regime, as discussed in Sec. 2.1.4.

2.3. Other Factors

Mesh Resolution per Mode. Our simulations use about 7.5 zones per initial bubble. Many reported simulations are somewhat more coarsely zoned. At these resolutions, the simulations are under resolved. Additional studies on the influence of mesh refinement would be desirable. The effect should be to produce a moderate increase in observed α_b , on the basis of experience in two dimensions.

Length of Domain. Waves reflecting from the ends of the computational domain can decrease the value of α_b according to two dimensional studies, especially if the domain boundary is too close to the edge of the mixing zone.

Compressibility. Compressibility has been observed to increase α_b moderately in two dimensional simulations [6]. We introduce the dimensionless parameter $M^2 = \lambda g/c_2^2$ where c_2 is the sound speed in the heavy fluid and λ is a mean bubble width, measured at the initial time, to characterize the compressibility of the flow. We correct for the effect of finite $M^2 > 0$ in Sec. 4.1.

Definition of Edge of Mixing Zone. The edge Z_k of the mixing zone is defined as the location of the furthest penetrating bubble ($k = 1$) or spike ($k = 2$), or equivalently the location of $\langle f_k \rangle = 0$. Here f_k is a local volume fraction and $\langle f_k \rangle$ is a transversely averaged volume fraction. This definition is inconvenient for untracked Eulerian simulation codes, as the mass diffusion extends the location of Z_k unrealistically under this definition. The definition has also been criticized as being statistically unstable in the limit of large ensemble size, *i.e.*, of many bubbles. For this reason, many simulations and some experiments report a definition of α_b based on 5% values, $\langle f_k \rangle = 0.05$. The 5% definition leads to a small decrease in α_b . For convenience of comparison, we report 0%, 1%, and 5% definitions of α_b .

The simulations based on shock capturing algorithms presented here use a level set function to determine locally in x, y, z, t a 50% contour, or zero-level surface to represent the interface. This contour can be used by any of the above methods to define global, *i.e.*, transverse averaged 0%, 1%, or 5% contours to determine the edge Z_b of the mixing zone and hence α_b . Only the 0% contours are reported for the capturing simulations.

Plainly these various definitions of Z_b and α_b are not identical (We observe about a 10% difference resulting from different definitions.) a fact which must be kept in mind when comparing simulations to one another or to experiment. See Sec. 4.1.

3. THE FRONT TRACKING ALGORITHM

The front tracking algorithm is described, in its 3D version, in recent publications [18, 17, 16]. This algorithm has been developed into a computer code *FrontTier*, see <http://www.ams.sunysb.edu/~shock/FTdoc.FTmain.html>. There are two essential ideas to the front tracking method. The first is the description of a front or interface as a lower dimensional structure, with supporting data structures and its own dynamics derived from the differential equation being solved. The second essential idea is to use (nonlocal) Riemann solvers to define the dynamics of the front, and ghost cell extrapolation to define a finite difference algorithm to couple the interior cells to the front.

The construction and redistribution of a three dimensional interface has been simplified [16] and is similar to but simpler than, Sethian's Fast Marching Algorithm [2, 1]. The grid based interface algorithm is narrower than Sethian's algorithm, being only one cell in width, and has no need for a supplementary partial differential equation to ensure isospacing of level contours, as there is only one contour, the interface itself.

3.1. Propagation of Front Points

The propagation of points on the front uses operator splitting in the directions normal and tangential to the interface. The latter operation projects the flow state onto the tangent plane at a point and then uses a finite difference or finite volume scheme to update the tangential component of Euler's equations. The former operation, called normal propagation, was described in [8]. Briefly, the Euler equations are projected into a one dimensional system along the normal ray from the point being propagated. A Riemann problem is solved using the two states at either side of the front as data to predict the front speed and compute a pair of updated states. One then uses the method of characteristics, tracing back linearly

from the predicted new front location, and the Rankine-Hugoniot conditions across the front to compute the time updated states at the front and a time updated front speed. The final front speed is computed using central differencing in time, *i.e.*, the average of the wave speed predicted from the initial Riemann problem and the value computed from the method of characteristics.

As an illustration of the method we consider the specific example of the propagation of a shock front from time t_0 to time $t_0 + \Delta t$ for Burger's equation:

$$u_t + \left(\frac{1}{2}u^2\right)_x = 0. \quad (19)$$

For simplicity we assume $t_0 = 0$, and that the initial shock is located at $x = 0$ so that our initial data is given by:

$$u(x, 0) = \begin{cases} u_l(x), & x < 0 \\ u_r(x), & 0 < x \end{cases}.$$

Let $s(t)$ be the shock location at time t , and define $u_-(t) = u(s(t)-, t)$, $u_+(t) = u(s(t)+, t)$. The Rankine-Hugoniot relations for Burger's equation imply that $\dot{s}(t) = \frac{1}{2}(u_-(t) + u_+(t))$, and since solutions to Burger's equation are constant along the characteristics $dx/dt = u$, we have $u_-(t) = u_l(s(t) - u_-(t)t)$ and $u_+(t) = u_r(s(t) - u_+(t)t)$. Differentiating these relations with respect to time we easily obtain:

$$\begin{aligned} \dot{u}_\pm(t) &= u'_{r,l} \{ \dot{s} - \dot{u}_\pm t - u_\pm \} \Big|_{(s(t), t)} \\ \ddot{u}_\pm(t) &= u''_{r,l} \{ \dot{s} - \dot{u}_\pm t - u_\pm \}^2 + u'_{r,l} \{ \ddot{s} - \ddot{u}_\pm t - 2\dot{u}_\pm \} \Big|_{(s(t), t)}. \end{aligned}$$

Using the standard notation $[a] = a_- - a_+$, and $\bar{a} = \frac{1}{2}(a_- + a_+)$, we obtain the derivatives at time $t = 0$:

$$\begin{aligned} \dot{u}_\pm(0) &= \pm \frac{1}{2} u'_{r,l} [u] \Big|_{(0,0)} \\ \ddot{u}_\pm(0) &= \frac{1}{4} u''_{r,l} [u]^2 \mp u'_{r,l} (u'_{r,l} \pm \frac{1}{4} [u']) [u] \Big|_{(0,0)} \\ \dot{s}(0) &= \bar{u} \Big|_{(0,0)} \\ \ddot{s}(0) &= -\frac{1}{4} [u'] [u] \Big|_{(0,0)} \\ \dot{\dot{s}}(0) &= \frac{1}{4} \{ \bar{u}'' [u] + 3\bar{u}' [u'] \} [u] \Big|_{(0,0)} \end{aligned}$$

The numerical solution at time Δt , as computed by the normal propagate algorithm, is easily shown to be:

$$\begin{aligned} u_\pm^n(\Delta t) &= u_{r,l} \left(\pm \frac{1}{2} [u(0)] \Delta t \right) \\ s^n(\Delta t) &= \frac{1}{2} (\bar{u}(0) + \bar{u}^n(\Delta t)) \Delta t. \end{aligned}$$

Expanding the numerical solution as a Taylor series in Δt and comparing this to the Taylor series for the exact solution we obtain:

$$\begin{aligned} |u_\pm^n(\Delta t) - u_\pm(\Delta t)| &= |u'_{r,l} (u'_{r,l} \pm \frac{1}{4} [u']) [u] \Big|_{(0,0)} \frac{\Delta t^2}{2} + \mathcal{O}(\Delta t^3) \\ |s^n(\Delta t) - s(\Delta t)| &= \left| \frac{1}{4} \bar{u}'' [u]^2 - \frac{3}{2} \bar{u}' [u'] [u] \Big|_{(0,0)} \frac{\Delta t^3}{3!} + \mathcal{O}(\Delta t^4) \right|, \end{aligned}$$

from which we conclude that the states at the front are correct to first order and the front position is correct to second order. It is interesting to note that the accuracy of the algorithm improves as the slopes on either side of the front approach zero with the states becoming second order accurate in the limit where the first derivatives vanish at the front.

3.2. Ghost Cell Extrapolation for Interior–Front Coupling

Since its inception, see [19], *FronTier* has used the ghost cell extrapolation algorithm to provide the coupling between the front and the interior system of states, and to update irregular cells, those whose regular finite difference stencil overlaps with the front. For cells with a regular stencil, a standard shock capturing scheme, such as a higher order Godunov method, is used.

For the cells with an irregular stencil, some cells of which are cut by the front, *FronTier* does not join states from different sides of the front with a finite difference operation. It was just such finite differences in the level set method [28] that were identified as an error [18]. Recent attempts to cure this error in the level set method [14] led to the adoption of the ghost cell method for level set propagation. However the absence of a Riemann solver to couple the states on the two sides of the interface was identified as a further source of error in this modified level set method [17].

We explain here the role of the Riemann solver for interior-front coupling. The Riemann solver enters into the front propagation itself and the setting of the front states, see Section 3.1. Given correctly computed front states, the ghost cell is extremely simple: extrapolation as a constant. States for each side of the front are extrapolated, to give locally double valued states near the front. Using these ghost cell states, and the regular states also, each cell, including the irregular ones, has a full stencil of states coming from a single side of the interface. The normal finite difference solver is called with these states, regular ones and the extrapolated ghost ones.

4. NEW SIMULATION RESULTS

All simulations reported here are performed on a $2 \times 2 \times 4$ computational domain with a $112 \times 112 \times 224$ grid. The initial interface is a perturbation of a planar $z = 0$ interface. The perturbation is defined by a sum of random Fourier modes, chosen as in Sec. 2 with $\lambda_{\max}/\lambda_{\min} = 2$ and Fourier modes with between 10 and 20 modes per linear dimension in the initial perturbation. This definition yields an initial array of about 15×15 bubbles in the perturbation and an average initial bubble width of 0.133. For *FronTier* simulations only, the initial velocities and other state variables are also perturbed, based on an analytic solution for the small amplitude (linearized) single mode Rayleigh-Taylor instability equations [15]. The amplitudes and phases are chosen by a random number generator, with independent normal distributions. The variance determines the overall amplitude of the interface perturbation, which we set as a multiple 0.0075 of the average initial bubble width. This amplitude is conservatively within the domain of the linearized Rayleigh-Taylor theory. Larger initial amplitudes are commonly used, meaning that the simulations are started in a nonlinear regime with strong transients. For reasons discussed in Sec. 2, a larger initial amplitude is used for the TVD simulations, and in this case, the initial amplitude per initial bubble width is approximately

0.0375. At this amplitude, there will be small but detectable nonlinear transient effects. Initial amplitudes are often reported in units of the full domain length, making the assessment of linear vs. nonlinear flow initialization difficult to assess. All simulations have an Atwood number $A = 0.5$, and except where varying the compressibility, an initial compressibility value $M^2 \equiv \lambda g/c_2^2 = 0.038$.

The three most important properties characterizing a mixing zone are its overall width, the distribution of mass or volume fraction across its width, and the degree of fine scale mixing. Here we analyze the simulations from these points of view.

4.1. *FrontTier* with Small Compressibility

We consider two values, both small, for the compressibility, $M^2 = 0.019$ and 0.038 . The purpose of this choice is to allow extrapolation to the incompressible limit $M^2 = 0$ in the determination of α_b . Extrapolation to the incompressible limit gives a reduction of about 10% in α_b from the larger of the two (small) values of compressibility, and results in agreement with experiment, see Tables 1, 2.

The late time interface separating heavy and light fluids is shown in Fig 1. The increase in α_b with compressibility was reported earlier in 2D simulations, [6], with an increase by up to a factor of 2 for $M^2 = 1.0$.

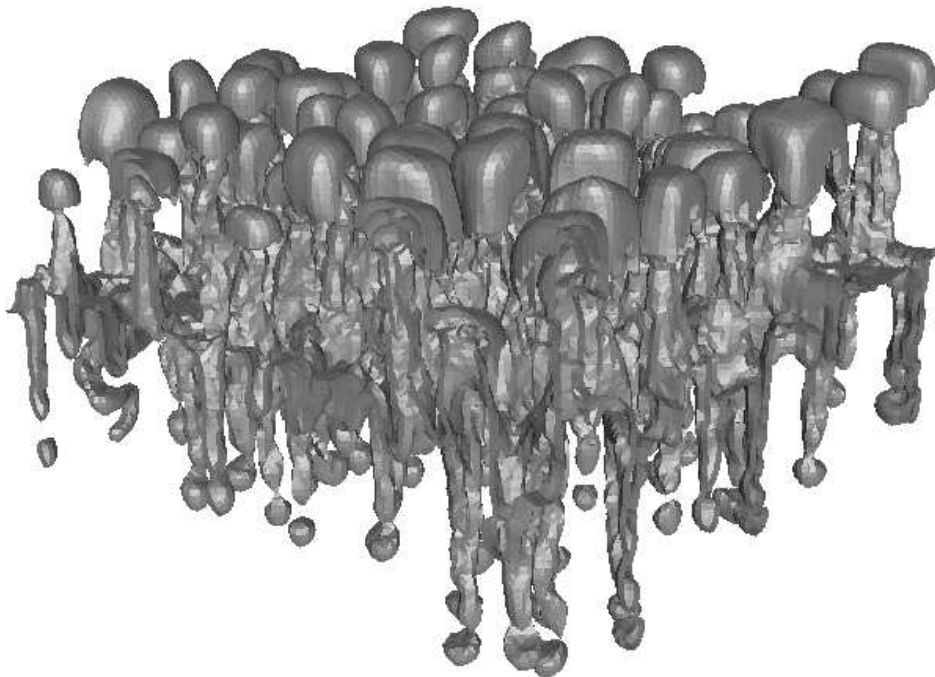


FIG. 1. A late time simulation of the Rayleigh-Taylor instability. The interface between the two fluids is shown. Here $M^2 = 0.038$.

The 5% contour method for computing α_b gives similar values, and a further reduction of 5% to 10% for α_b . The resulting (lower) value of α_b for *FrontTier* simulations probably improves the agreement with experiment. Results are presented in Table 2. Data for the computation of α_b from the simulation of Fig. 1 is given

TABLE 2
 Values for α_b as determined by *FronTier*. Comparison of the effects of three definitions of α_b . Values of α_b for compressible flow and extrapolation to $M^2 = 0$.

M^2	Definitions of α_b		
	0%	1%	5%
0.038	0.083	0.078	0.070
0.019	0.076	0.074	0.068
0 (Extrap.)	0.069	0.070	0.066

in Fig 2. We assign error bounds of $\pm 5\%$ due to data analysis in the numerical determination of α_b . Other possible systematic errors in the simulation, such as grid resolution, are discussed in Sec. 2.

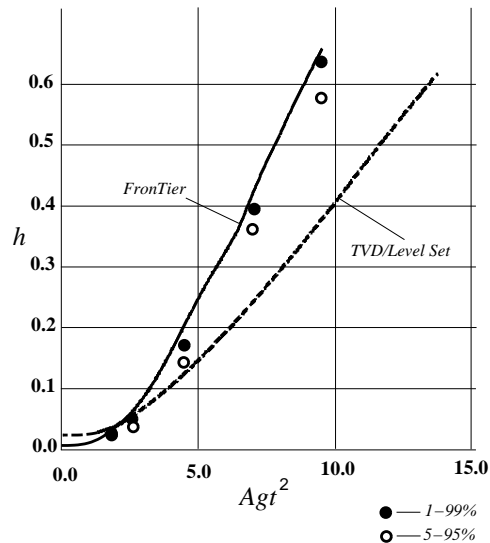


FIG. 2. Height *vs.* Agt^2 . Here the solid line is the 0% definition for the *FronTier* simulation and the dashed line comes from the TVD simulation. The black circles are the 1% definition, and the open circles result from the 5% definition, for the *FronTier* simulation.

4.2. TVD with and without Artificial Compression

Here we show the influence of dissipative effects, by comparing a *FronTier* (tracked) simulation with two TVD (capturing) simulations. We duplicate earlier reported capturing growth rates for comparable simulation times and ensemble sizes. Of the factor of two variation in principal simulation values for α_b , about half appears at the simulation times reported here. Our results explain this half quantitatively as due to the dissipative effects of capturing algorithms. By comparing TVD to *Fron*

TABLE 3
Dependence of α_b on numerical diffusion and viscosity

Method	Observed Numerical Diffusion Length	α_b (0%; Compressible)
<i>FronTier</i>	0 cells	0.083
AC	6-7 cells	0.053
TVD	11 cells	0.050

Tier, we infer that diffusion of interfacial vorticity and density jumps is significant, accounting for a 40% decrease in α_b , and about half of the total discrepancy with most capturing simulations. By comparing two different capturing simulations, one with artificial compression (AC) to limit mass diffusion, we infer that the major dissipative effect is viscosity. An alternate explanation is that the AC algorithm, being less effective in its nonlinear application, does not sufficiently control mass diffusion. For the purpose of this comparison, we keep the compressibility fixed at $M^2 = 0.038$. All inputs and sensitive factors (except as explicitly noted) are the same as for the *FronTier* simulations, so the differences which result can be attributed to dissipative effects of the TVD capturing algorithm. The comparable incompressible values of α_b and the effect of different definitions of α_b are shown in Table 2 and summarized in Table 3. The tabulated numerical diffusion length is the local width of the numerically defined interface, as determined at a middle value of t , $t = 6$, out of a total simulation time of $t = 12$. Observe that this length is comparable to the size of the bubbles and spikes in the flow for the two capturing algorithms. Artificial compression reduces this length by half.

4.3. Fine Scale vs. Chunk Mix

4.3.1. Numerical Mixing Fraction

We introduce the local volume fraction $f_k(x, y, z, t)$ as the fraction of fluid k at the space-time location x, y, z, t . The numerical mixing fraction is defined [41] by the transverse (and ensemble) averaged correlation

$$\theta(z, t) = \frac{\langle f_1 f_2 \rangle}{\langle f_1 \rangle \langle f_2 \rangle}. \quad (20)$$

Youngs [41] reports mixing fractions $\theta \approx 0.8$ for a van Leer advection algorithm, indicating nearly perfect numerical mixing. *FronTier*, with zero mass diffusion across a tracked interface, has $\theta \equiv 0$. The Dimonte-Schneider experiments, performed with immiscible fluids, have a mixing fraction $\theta = 0$. Youngs' experiments used both miscible and immiscible fluids.

4.3.2. The Coherence Correlation Length

This section presents an initial attempt to compare simulations and experiments at lengths intermediate between the chunk mix length of the mixing zone itself and the diffusive length scale of molecular mixing. Such length scales may originate

from the breakup of large scale structures into smaller ones. See also the turbulence based analysis of [9]. We start with the observation that the coherence probability, *i.e.*, the probability to remain within a single phase while moving on a straight line, satisfies an exponential fall off with distance. The characteristic length λ for this decay is called the coherence length.

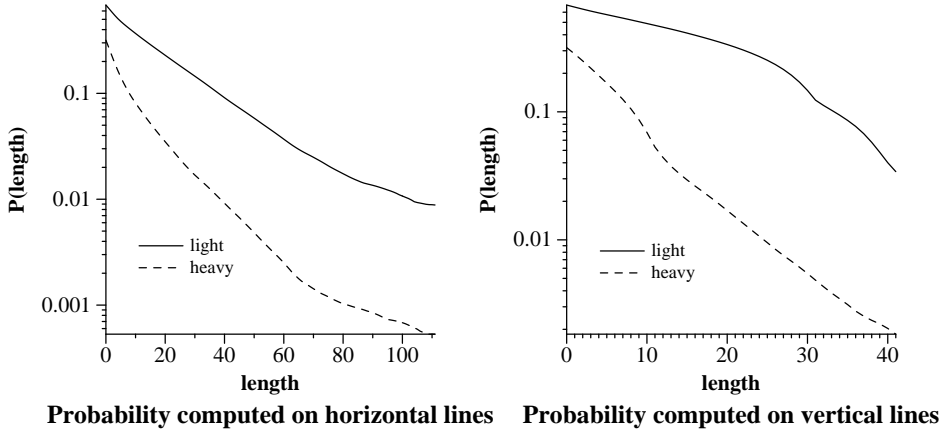


FIG. 3. Exponential rate laws for the probability of an interval of length l to lie totally within a specified phase, determined from *Frontier* simulations reported here. The data are well fit to an exponential law $\exp(-l/\lambda)$ over two orders of magnitude in probability.

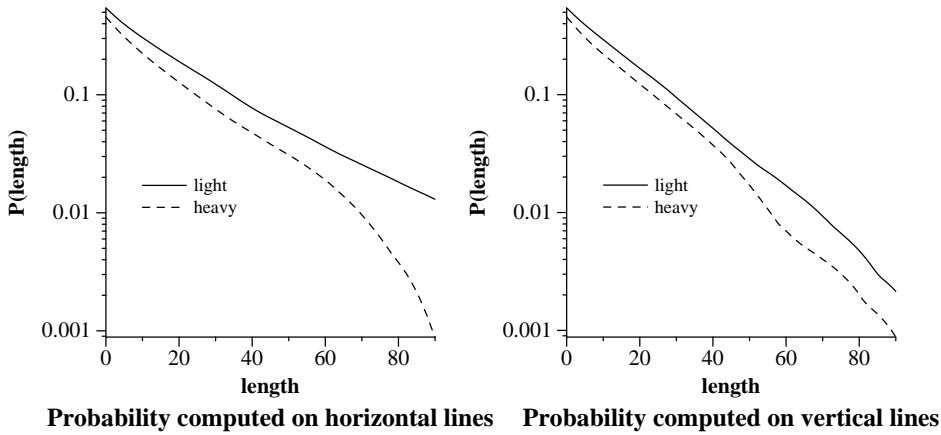


FIG. 4. Exponential rate laws for the probability of an interval of length l to lie totally within a specified phase as determined experimentally [11].

The exponential law for the coherence pdf can be seen in simulations, Fig. 3, and experiments [11], Fig. 4. The exponential structure for the pdf is equivalent to a Poisson process for phase boundaries encountered for motion along a straight line, and thus to a Markov property for the binary random field defined by the two phase flow. This fact leads to an elegant mathematical description of various transition probabilities [30].

Table 4 lists coherence lengths as extracted from both simulation and experiment. The experimental data is generated from the central half of the mixing zone only.

TABLE 4
Experimental and simulation values for the coherence length scale in
a Markov random field description of the interface statistics.

	Experiment	Experiment	Simulation	Simulation
	Late Time	Early Time	Late Time	Early Time
λ_h				
Light Fluid	24	12	23	22
Heavy Fluid	19	19	15	24
λ_v				
Light Fluid	17	10	29	5
Heavy Fluid	15	13	6	7

However, due to the narrowness of the simulation mixing zone, a larger central region was used to construct the simulation data. We note the important fact that the coherence length does not scale with t^2 or the width of the mixing zone, that changes by a factor of 3 between the two experimental times shown in Table 4 and by a factor of 2 for the simulation times. Thus it must describe a new length scale and the possible beginning of a new flow regime. The coherence pdf should not be confused with the bubble size pdf, that also satisfies an exponential law [4] but obeys a t^2 scaling.

The experimental and simulation numbers are roughly similar but should not be compared. The early and late simulation times are both much earlier than the early experimental time, in terms of mixing zone evolution. Also an initial perturbation length scale, which might set the length scale for the coherence lengths, is not measured for the experiment, so units for comparison of lengths are not known.

We note trends for growth of the experimental light fluid but not the heavy fluid coherence lengths, and a trend for growth of the light fluid vertical simulation coherence length. Since the observational times for these trends are not comparable, we draw no conclusions at this time.

5. CONCLUSIONS

We have analyzed the mixing growth rate constant α_b in multi-mode (random) Rayleigh-Taylor instability in a 3D planar geometry. In spite of the large effort made to obtain values for this quantity, disagreements and inconsistencies have persisted.

We identified two significant factors which are sufficient to obtain *FrontTier* simulations that agree with experimental data. The first factor is a correction for compressibility and the second is a correction for differing definitions of the constant α_b .

The numerical dissipation of the capturing algorithms is a significant factor, sufficient to explain part of the spread in simulation values, and probably all of the principal discrepancies observed up to the simulation times studied here. See

Table 1. For the simulation times and ensemble sizes explored, numerical viscosity appears to play a larger role than numerical mass diffusion. See Table 3.

We have begun an exploration of new physical length scales, which could signal a transition to a new flow regime for Rayleigh-Taylor mixing.

Further studies are needed to resolve remaining issues, including refinement of the mesh per mode, increase in the number of modes, and simulations carried to later time. The present paper provides a perspective on, but does not definitively resolve, the causes of the discrepancies concerning the growth rate α_b . For this reason we list some outstanding questions, and propose possible research which could help to resolve remaining questions.

1. To what extent can long wave length noise in the experiments contribute to the experimental value of α_b ? How rigid a restriction on the noise spectrum is the observed growth of $Z_1(t)$ scaling linearly in t^2 over the experimental time periods? Experimental characterization of initial conditions would contribute to a resolution of this issue.

2. The decreasing, time dependent simulation values of α_b for capturing algorithms signals a new length scale to break the t^2 scaling law. We propose here that this length scale originates in numerical dissipation. The Lattice Boltzmann algorithm allows a controlled variation of viscosity. Parametric studies with this algorithm could determine the influence of viscosity upon α_b .

3. The 40% difference reported here between the TVD algorithm and *FronTier*, when run to identical times, and with identical resolution, indicates that dissipation is significant, and sufficient to explain the principal discrepancies among simulations up to the simulation times reported here. We propose to run *FronTier* simulations to later time to determine the value of α_b which results.

REFERENCES

1. D. Adalsteinson and J. A. Sethian. The fast construction of extension velocities in level set methods. *J. Comp. Phys.*, 1998. submitted.
2. D. Adalsteinsson, R. Kimmel, R. Malladi, and J. A. Sethian. Fast marching methods for computing solutions to static Hamilton-Jacobi equations. Technical Report preprint PAM-667, Univ. Cal., Berkeley, 1996.
3. U. Alon, J. Hecht, D. Mukamel, and D. Shvarts. Scale invariant mixing rates of hydrodynamically unstable interfaces. *Phys. Rev. Lett.*, 72:2867–2870, 1994.
4. U. Alon, D. Shvartz, and D. Mukard. Scale-invariant regime in Rayleigh-Taylor bubble-front dynamics. *Phys. Rev. E*, 48:1008–1014, 1993.
5. A. Blair, N. Metropolis, J. von Neuman, A. H. Taub, and M. Tsingou. A study of a numerical solution to a two-dimensional hydrodynamic problem. *Mathematical Tables and other Aids to Computation*, 13:145–184, 1959.
6. Y. Chen, Y. Deng, J. Glimm, G. Li, D. H. Sharp, and Q. Zhang. A renormalization group scaling analysis for compressible two-phase flow. *Phys. Fluids A*, 5(11):2929–2937, 1993.
7. B. Cheng, J. Glimm, X. L. Li, and D. H. Sharp. Subgrid models and DNS studies of fluid mixing. In *Proceedings of the 7th International Conference on the Physics of Compressible Turbulent Mixing, (1999)*, 2000. submitted.
8. I-L. Chern, J. Glimm, O. McBryan, B. Plohr, and S. Yaniv. Front tracking for gas dynamics. *J. Comput. Phys.*, 62:83–110, 1986.
9. S. B. Dalziel, P. F. Linden, and D. L. Youngs. Self-similarity and internal structure of turbulence induced by Rayleigh-Taylor instability. *J. Fluid Mech.*, 1999. to appear.

10. Dimits. Private communication. Technical report, 1999.
11. G. Dimonte and M. Schneider. Density ratio dependence of Rayleigh-Taylor mixing for sustained and impulsive acceleration histories. Technical report, Lawrence Livermore National Laboratory, 1999. submitted to Phys. Fluids.
12. D. Drew and S. Passman. *Theory of Multicomponent Fluids*. Applied Mathematical Sciences. Springer-Verlag, New York, 1999.
13. R. E. Duff, F. H. Harlow, and C. W. Hirt. Effects of diffusion on interface instability between gases. *Phys. of Fluids*, 5:417–425, 1962.
14. R. P. Fedkiw, T. Aslam, B. Merriman, and S. Osher. A non-oscillatory Eulerian approach to interfaces in multimaterial flows (the ghost fluid method). *J. Comp. Phys.*, 1998. Submitted.
15. C. L. Gardner, J. Glimm, J. Grove, O. McBryan, R. Menikoff, D. H. Sharp, and Q. Zhang. A study of chaos and mixing in Rayleigh-Taylor and Richtmyer-Meshkov unstable interfaces. In M. Duong-van and B. Nichols, editors, *Proceedings of the International Conference on 'The Physics of Chaos and Systems Far from Equilibrium' (CHAOS' 87), Monterey, CA, USA, Jan. 11–14, 1987*. 1988. Special Issue of Nuclear Physics B (proceedings supplements section).
16. J. Glimm, J. Grove, X. L. Li, and D. C. Tan. Robust computational algorithms for dynamic interface tracking in three dimensions. *SIAM J. Sci. Comp.*, 1999. In Press, SUNYSB-AMS-98-03 and LA-UR-99-1780.
17. J. Glimm, J. Grove, X. L. Li, and N. Zhao. Simple front tracking. In G.-Q. Chen and E. DiBenedetto, editors, *Contemporary Mathematics*, volume 238. Amer. Math. Soc., Providence, RI, 1999. To appear, SUNYSB-AMS-98-12 and LANL report LA-UR 99787.
18. J. Glimm, J. W. Grove, X.-L. Li, K.-M. Shyue, Q. Zhang, and Y. Zeng. Three dimensional front tracking. *SIAM J. Sci. Comp.*, 19:703–727, 1998.
19. J. Glimm, D. Marchesin, and O. McBryan. Subgrid resolution of fluid discontinuities II. *J. Comput. Phys.*, 37:336–354, 1980.
20. J. Glimm and D. H. Sharp. Chaotic mixing as a renormalization group fixed point. *Phys. Rev. Lett.*, 64:2137–2139, 1990.
21. J. Glimm and D. H. Sharp. Stochastic partial differential equations: Selected applications in continuum physics. In R. A. Carmona and B. L. Rozovskii, editors, *Stochastic Partial Differential Equations: Six Perspectives*, Mathematical Surveys and Monographs. American Mathematical Society, Providence, 1997.
22. E. Godlewski and P. A. Raviart. *Numerical Approximation of Hyperbolic Systems of Conservation Laws*. Springer Verlag, New York, 1991.
23. G. Hedstrom. Models of difference schemes for $u_t + u_x = 0$ by partial differential equations. *Mat. Comp.*, 29:969–977, 1975.
24. Ya. Kucherenko, L. I. Shbarshev, V. I. Chitaikin, S. A. Balabin, and A. P. Palaev. Experimental investigation into the self-similar mode of the gravitational turbulent mixing. In *Proceedings of the 3rd International Workshop on the Physics Compressible Turbulent Mixing*. 1991.
25. R. LeVeque. *Numerical Methods for Conservation Laws*. Birkhäuser Verlag, Basel–Boston–Berlin, 1992.
26. X.-L. Li, B. X. Jin, and J. Glimm. Numerical study for the three dimensional Rayleigh-Taylor instability using the TVD/AC scheme and parallel computation. *J. Comp. Phys.*, 126:343–355, 1996.
27. P. F. Linden, J. M. Redondo, and D. L. Youngs. Molecular mixing in Rayleigh-Taylor instability. *J. Fluid Mech.*, 265:97–124, 1994.
28. R. Mulder, S. Osher, and J. A. Sethian. Computing interface motion in compressible gas dynamics. *J. Comp. Phys.*, 100:209–228, 1992.
29. Oparin. Private communication. Technical report, 1999.
30. G. C. Pomraning. Transport theory in discrete stochastic mixtures. *Advances in Nuclear Science and Technology*, 24:47–93, 1996.
31. Lord Rayleigh. Investigation of the character of the equilibrium of an incompressible heavy fluid of variable density. In *Scientific Papers*, volume II, page 200. Cambridge Univ. Press, Cambridge, England, 1900.
32. K. I. Read. Experimental investigation of turbulent mixing by Rayleigh-Taylor instability. *Physica D*, 12:45–58, 1984.

33. R. Richtmyer and K. Morton. *Difference Methods for Initial Value Problems*. Interscience, New York, second edition, 1967.
34. M. B. Schneider, G. Dimonte, and B. Remington. Large and small scale structure in Rayleigh-Taylor mixing. *Phys. Rev. Lett.*, 80(16):3507–3510, 1998.
35. D. H. Sharp. An overview of Rayleigh-Taylor instability. *Physica D*, 12:3–18, 1984.
36. D. H. Sharp and J. A. Wheeler. Late stage of Rayleigh-Taylor instability. Technical report, Institute of Defense Analyses, 1961. Unpublished Technical Report.
37. D. M. Snider and M. J. Andrews. Rayleigh-Taylor and shear driven mixing with an unstable thermal stratification. *Phys. Fluids*, 6(10):3324–3334, 1994.
38. G. I. Taylor. The instability of liquid surfaces when accelerated in a direction perpendicular to their planes I. *Proc. R. Soc. London A*, 201:192–196, 1950.
39. R. Warming and Hyett. The modified equation approach to the stability and accuracy analysis of finite-difference methods. *J. Comp. Phys.*, 14:159–179, 1974.
40. D. L. Youngs. Numerical simulation of turbulent mixing by Rayleigh-Taylor instability. *Physica D*, 12:32–44, 1984.
41. D. L. Youngs. Three-dimensional numerical simulation of turbulent mixing by Rayleigh-Taylor instability. *Phys. Fluids A*, 3:1312–1319, 1991.
42. D. L. Youngs. Private communication. Technical report, 1999.
43. Q. Zhang. Validation of the chaotic mixing renormalization group fixed point. *Phys. Lett. A*, 151:18–22, 1990.